Electronic Supplementary Information

Tunable Intermediate-Logic Ternary Circuits based on $MoSe_2$-WSe_2 Heterojunction

*Seongin Hong[1, ‡], Hyeon Jung Park[1, ‡], Hae Won Cho[1], Junwoo Park[1], Sunkook Kim[1, *], and Hocheon Yoo[2, *]*

[1] School of Advanced Materials Science and Engineering, Sungkyunkwan University, Suwon, Gyeonggi-do, 16419, Republic of Korea

[2] Department of Electronic Engineering, Gachon University, 1342 Seongnam-daero, Seongnam 13120, Republic of Korea

Correspondence and requests for materials should be addressed to S. K. (email: intel0616@gmail.com) or H. Y. (email: hyoo@gachon.ac.kr).

Table S1. Field effect mobility of the WSe_2, $MoSe_2$, and $MoSe_2$-WSe_2 vdW-H.

Channel layer	Linear regime (lV_Dl = 1 V)		Saturation regime (lV_Dl = 20 V)	
	$\mu_{electron}$ ($cm^2V^{-1}s^{-1}$)	μ_{hole} ($cm^2V^{-1}s^{-1}$)	$\mu_{electron}$ ($cm^2V^{-1}s^{-1}$)	μ_{hole} ($cm^2V^{-1}s^{-1}$)
$MoSe_2$	46.79	0.04	20.62	0.23
WSe_2	1.63	34.47	2.39	24.36

Field effect mobility (μ_{eff}) is one of the parameters for evaluating the performance of transistors. It can be extracted from $\boldsymbol{\mu_{eff}} = \frac{\partial I_D}{\partial V_G}\frac{L}{W}\frac{I}{C_{ox}V_D}$, where L and W are the channel length and width, respectively, and C_{ox} is the capacitance of the gate insulator.[S1] Regarding the drain voltage applied to the $MoSe_2$-WSe_2 vdW-H transistor in Figure 1e, μ_{eff} is extracted from the saturated drain current (V_D = −20 V). The calculated μ_{eff} of the baseline $MoSe_2$ and WSe_2 transistors as a function of V_G is shown In Table S1. As a result, the $MoSe_2$ and WSe_2 transistors exhibit n-type dominant and p-type dominant behaviors, respectively.

Table S2. Comparison of the proposed H-TR with previous studies on heterojunction transistors for ternary inverter operation.

P-type material (or ambipolar)	N-type materials (or ambipolar)	Dielectric	g_m [μ S/F]	Negative g_m region [V]	Year	Ref.
WSe_2 (ambipolar)	MoS_2	HfO_2	No length	~0.1	2016	[22]
Graphene	Graphene	SiO_2	No length	~20	2016	[38]
WSe_2	Graphene	SiO_2	$\sim -4.3 \times 10^{-4}$	~15	2017	[19]
Black phosphorus (ambipolar)	MoS_2	HfSiO	$\sim -1.2 \times 10^{-5}$	~1.5	2017	[18]
Black phosphorus	SnSeS	HfO_2	$\sim -1.4 \times 10^{-4}$	~2	2018	[29]
Graphene	R6G /graphene	ODTS/SiO_2	$\sim -2.6 \times 10^{-3}$	~18	2018	[27]
$MoTe_2$	MoS_2	h-BN/SiO_2	-	~20	2019	[28]
$MoTe_2$	MoS_2	SiO_2	$\sim -6.4 \times 10^{-7}$	~8	2019	[26]
Graphene	Graphene	SiO_2	$\sim -1.7 \times 10^{-2}$	~13	2019	[39]
Black phosphorus (ambipolar)	ReS_2	HfO_2	$\sim -1.7 \times 10^{-3}$	~2	2020	[23]
Black phosphorus	MoS_2	SiO_2	$\sim -1.8 \times 10^{-4}$	~10	2020	[42]
WSe_2	ReS_2	SiO_2	$\sim -1.5 \times 10^{-4}$	~43	2020	[43]
WSe_2 (ambipolar)	$MoSe_2$ (ambipolar)	SiO_2	$\sim -1.1 \times 10^{-2}$	~45	2020	This work

Table S3. Comparison of the T-inverter with previous studies on ternary inverters.

Pull-up transistor	Pull-down transistor	Output swing	Pulsed measurement	Middle logic state [V]	Tunability of intermediate-state	Ref.
WSe_2	WSe_2/MoS_2 C-Hetero	~75%	X	0.7	X	[22]
Graphene	Graphene	~40%	X	0.6	X	[38]
BP	BP/ ReS_2 C-Hetero	~75%	X	4	X	[25]
BP	Graphene/ Wse_2	~75%	X	15	X	[19]
BP	BP/MoS_2 C-Hetero	~90%	X	0.4	X	[18]
BP	BP/SnSeS	~50%	X	1.2	X	[29]
Graphene/R6G/ graphene	R6G/ graphene	~10%	X	20	X	[27]
$MoTe_2$	$MoTe_2/MoS_2$	~70%	X	9	X	[28]
$MoTe_2$	$MoTe_2/MoS_2$	~60%	X	18	X	[26]
$ReSe_2$	IGZO	~97%	O	1.5	X	[30]
BP	BP/ReS_2	~90%	O	1.5	X	[23]
BP	BP/MoS_2	~40%	X	5	X	[42]
$MoSe_2/WSe_2$	MoS_2	~100%	O	34	O	This work

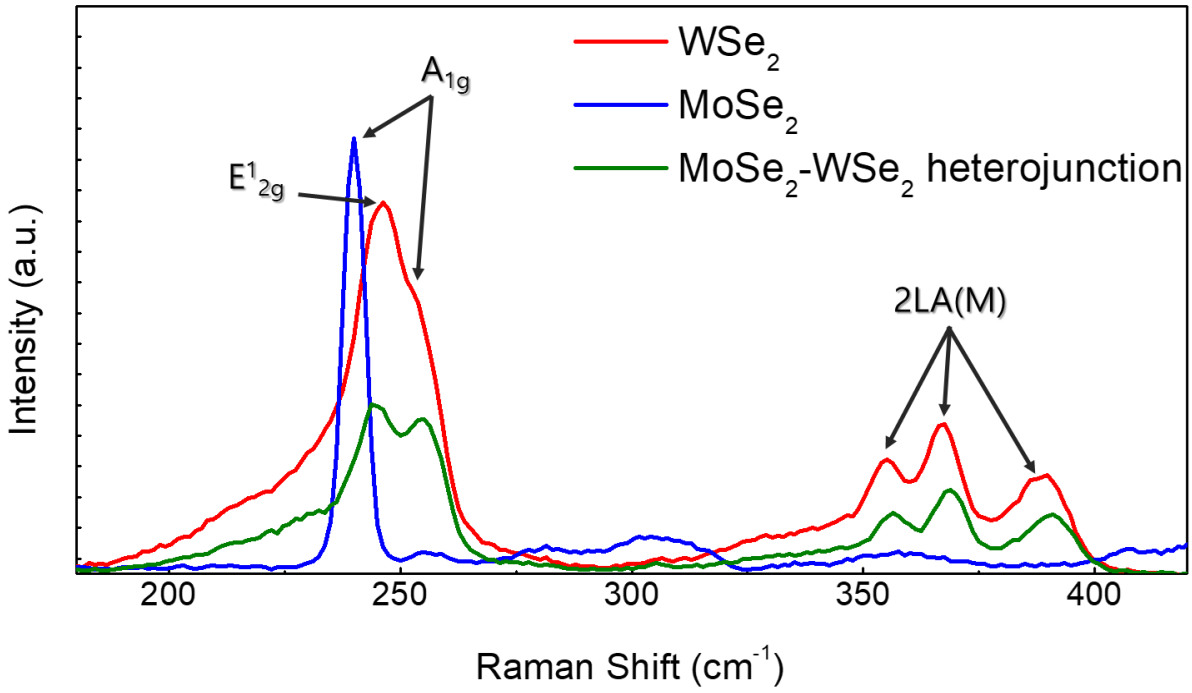

Figure S1. Raman spectra of WSe_2, $MoSe_2$, and $MoSe_2$-WSe_2 vdW-H. The Raman spectra were measured at three different positions of the WSe_2, $MoSe_2$, and $MoSe_2$-WSe_2 vdW-H regions as shown in Figure S1. The observed Raman peaks (red curve) of the WSe_2 at 246.3 and 253.8 cm^{-1} correspond to the E^1_{2g} and A_{1g} vibrational modes, respectively. The E^1_{2g} mode arises from the vibrations involved in both W and Se atoms in the basal plane. These vibrations are in the opposite directions from each other.[S2,3] The A_{1g} mode refers only to the vibrations of the Se atoms along the perpendicular to plan. The other peaks (2LA (M) modes) are the second-order Raman mode due to LA (longitudinal acoustic) phonons at the M point in the Brillouin zone and combinational Raman modes.[S2,3] The Raman peak of $MoSe_2$ (blue curve) was observed at 239.9 cm^{-1} corresponding to the A_{1g} modes due to the out-of-plane vibration. In-plane vibration was not observed.[S4] In the $MoSe_2$-WSe_2 region, the Raman peaks corresponding to both WSe_2 and $MoSe_2$ appeared and there was no significant shift of these peaks. This supports that the $MoSe_2$-WSe_2 was having van der Waals interaction without the new bond between the WSe_2 and $MoSe_2$.

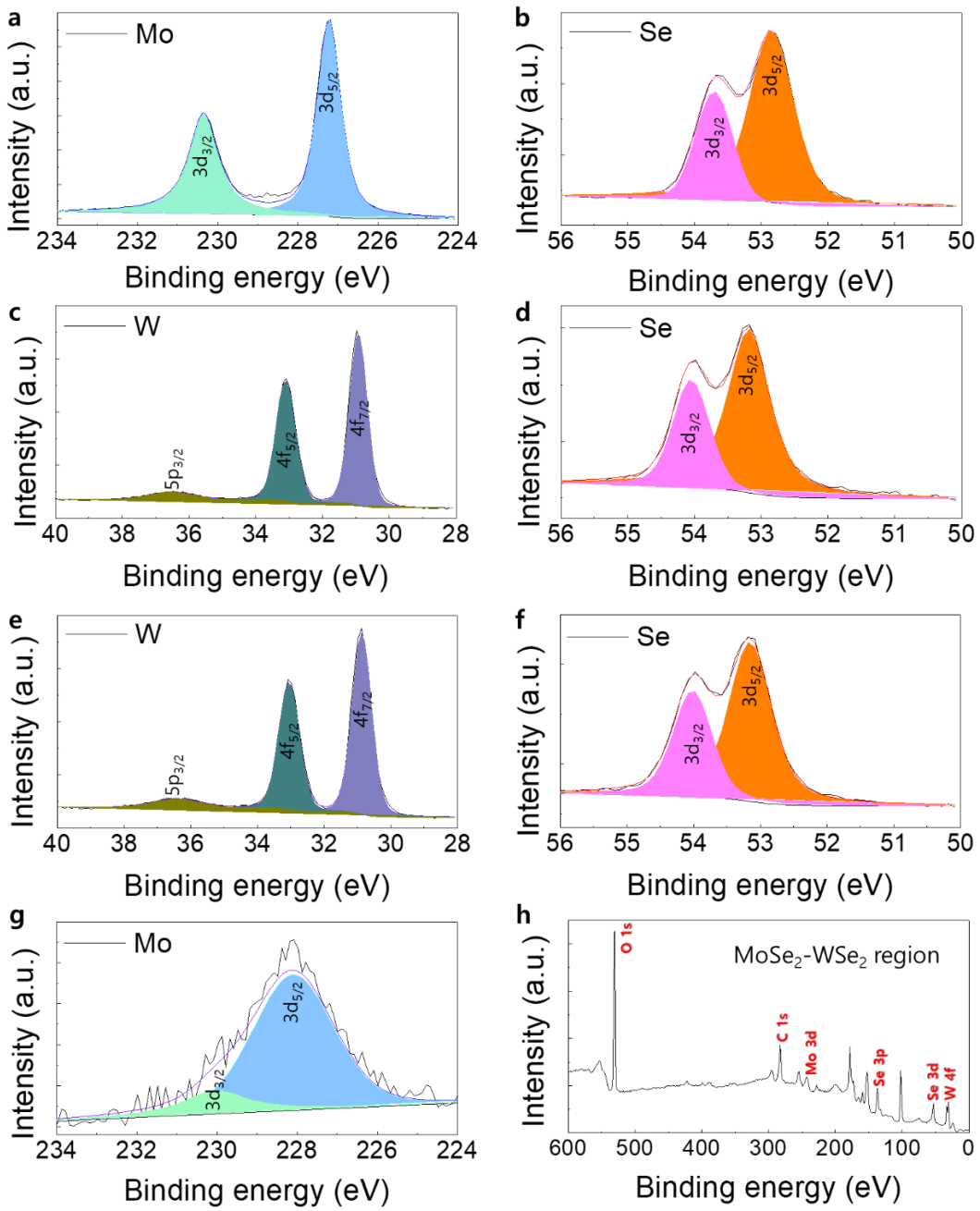

Figure S2. XPS spectra of WSe_2, $MoSe_2$, and $MoSe_2$-WSe_2 vdW-H. a) Mo 3d and b) Se 3d binding energies for $MoSe_2$. c) W 4f, 5p and d) Se 3d binding energies for WSe_2. e) W 4f, 5p, f) Se 3d, g) Mo 3d, and h) XPS survey scans for the $MoSe_2$-WSe_2 vdW-H region. X-ray photoelectron spectroscopy (XPS) was applied to examine the binding energies of $MoSe_2$, WSe_2, and the $MoSe_2$-WSe_2 vdW-H. For the WSe_2, the observed peaks of W at 30.8 and 33.0 eV correspond to the $4f_{7/2}$ and $4f_{5/2}$ binding energies, respectively, and the observed peak at 36.4 eV corresponds to the $5p_{3/2}$ binding energy. Two peaks representing the $3d_{5/2}$ and $3d_{3/2}$ binding energies

of Se are observed at 53.1 and 54.8 eV, respectively (Figure S2a and S2b).[S5,6] For the $MoSe_2$, the observed double peaks of Mo at 227.2 and 230.2 eV correspond to the $3d_{5/2}$ and $3d_{3/2}$ binding energies, respectively. The two peaks of Se corresponding to the $3d_{5/2}$ and $3d_{3/2}$ binding energies observed at 52.8 and 53.6 eV, respectively (Figure S2c and S2d).[S5,6] In the $MoSe_2$-WSe_2 vdW-H region, all three elements (W, Se, and Mo) were observed. The two peaks representing the $4f_{7/2}$ and $4f_{5/2}$ binding energies of W are observed at 30.8 and 33.0 eV, respectively (Figure S2e). Two peaks corresponding to the $3d_{5/2}$ and $3d_{3/2}$ binding energies of Se are observed at 53.0 and 54.0 eV, respectively (Figure S2f). The $3d_{5/2}$ and $3d_{3/2}$ binding energies of Mo are weakly observed at 228.0 and 230.0 eV, respectively. The presence of W, Mo, and Se elements was clearly confirmed through the XPS survey scan (Figure S2g and S2h).

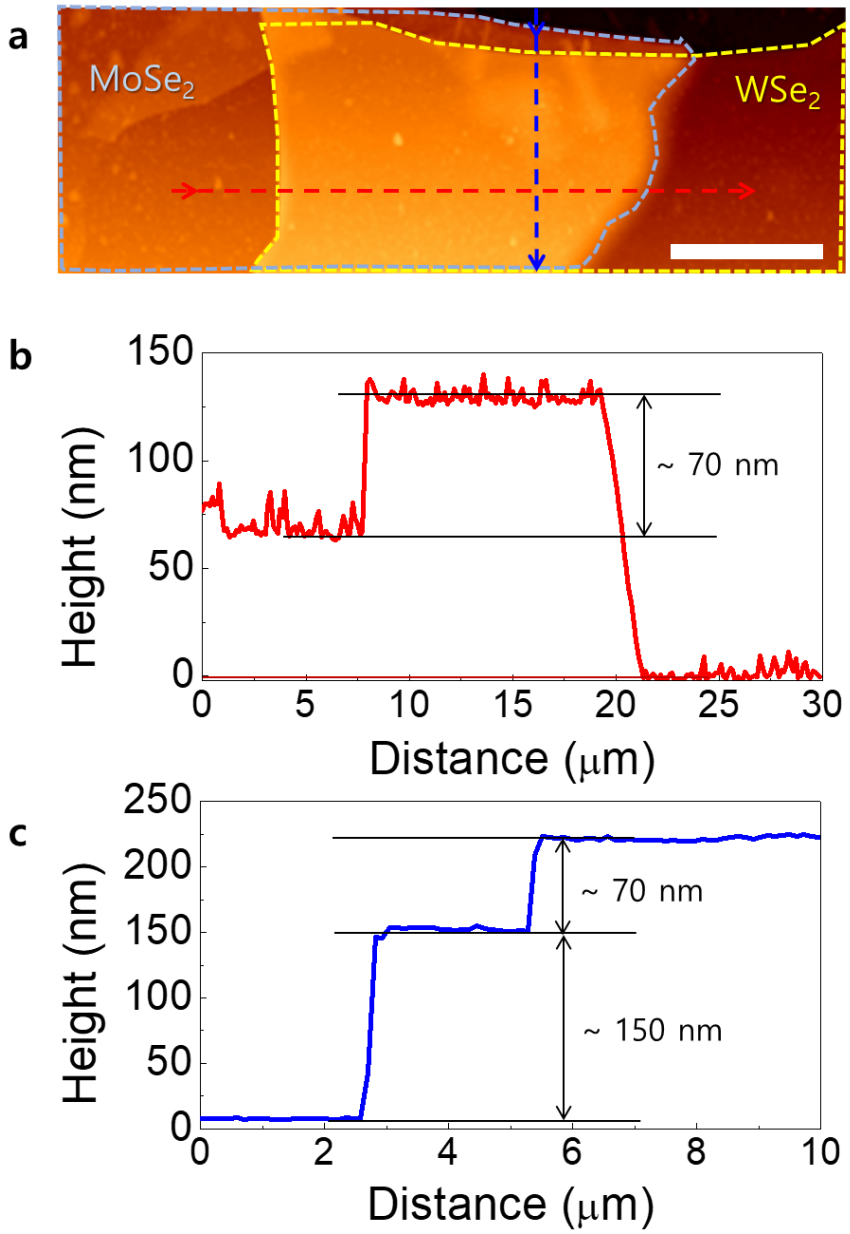

Figure S3. Thickness of $MoSe_2$ and WSe_2 vdW-H. a) AFM image of the $MoSe_2$ (grey dashed line)-WSe_2 (yellow dashed line) vdW-H. The length of the scale bar is 5μm. Cross-section profile along b) red dashed line (x-axis scan) and c) blue dashed line (y-axis scan) in the AFM image of $MoSe_2$-WSe_2 vdW-H. The thicknesses of the WSe_2 and $MoSe_2$ were measured to be about 70 and 150 nm, respectively, using the profile (blue dashed line) of the AFM image.

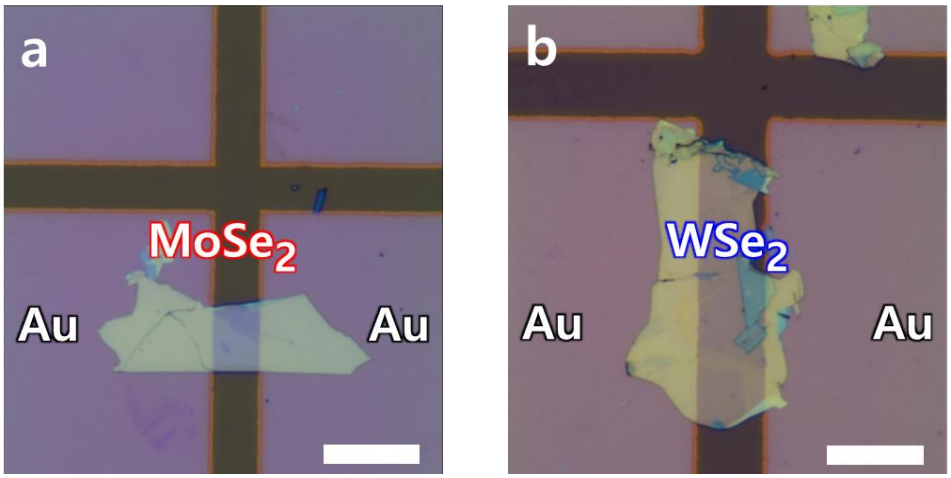

Figure S4. Optical microscope images of a) baseline $MoSe_2$ transistor and b) baseline WSe_2 transistor. The length of the scale bar is 30um.

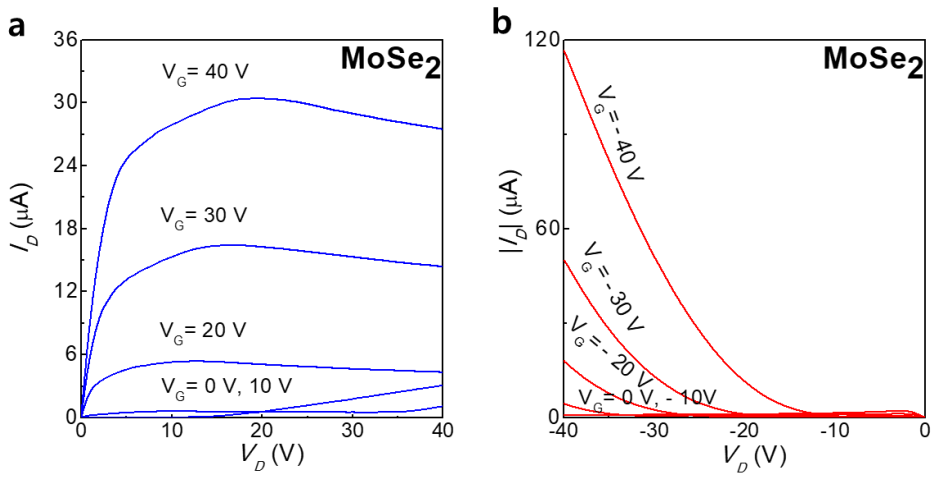

Figure S5. Output characteristics of the baseline $MoSe_2$ transistor a) for V_D = 0 to 40 V and V_G = 0, 10, 20, 30, and 40 V and b) for V_D = 0 to −40 V and V_G = 0, −10, −20, −30, and −40 V.

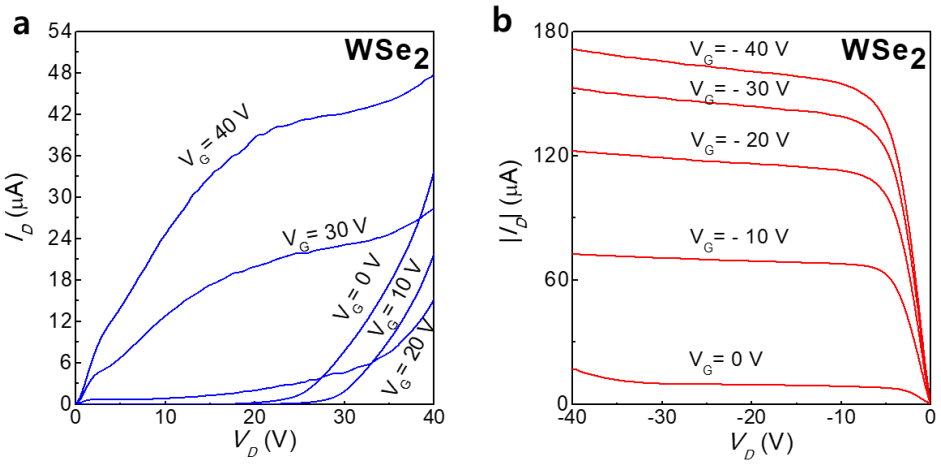

Figure S6. Output characteristics of the baseline WSe_2 transistor a) for V_D = 0 to 40 V and V_G = 0, 10, 20, 30, and 40 V and b) for V_D = 0 to −40 V and V_G = 0, −10, −20, −30, and −40 V.

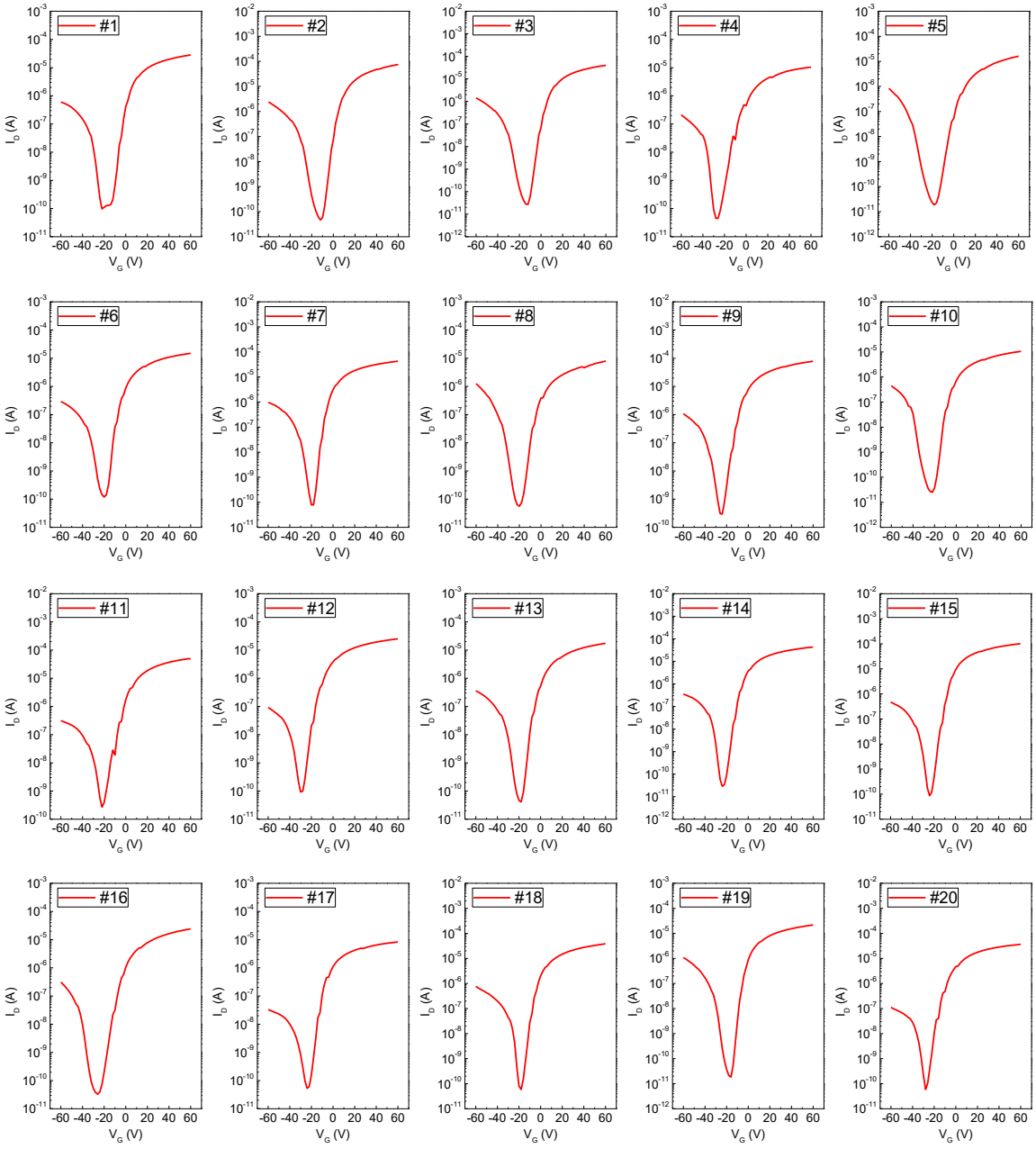

Figure S7. Transfer characteristics of 20 baseline $MoSe_2$ transistors.

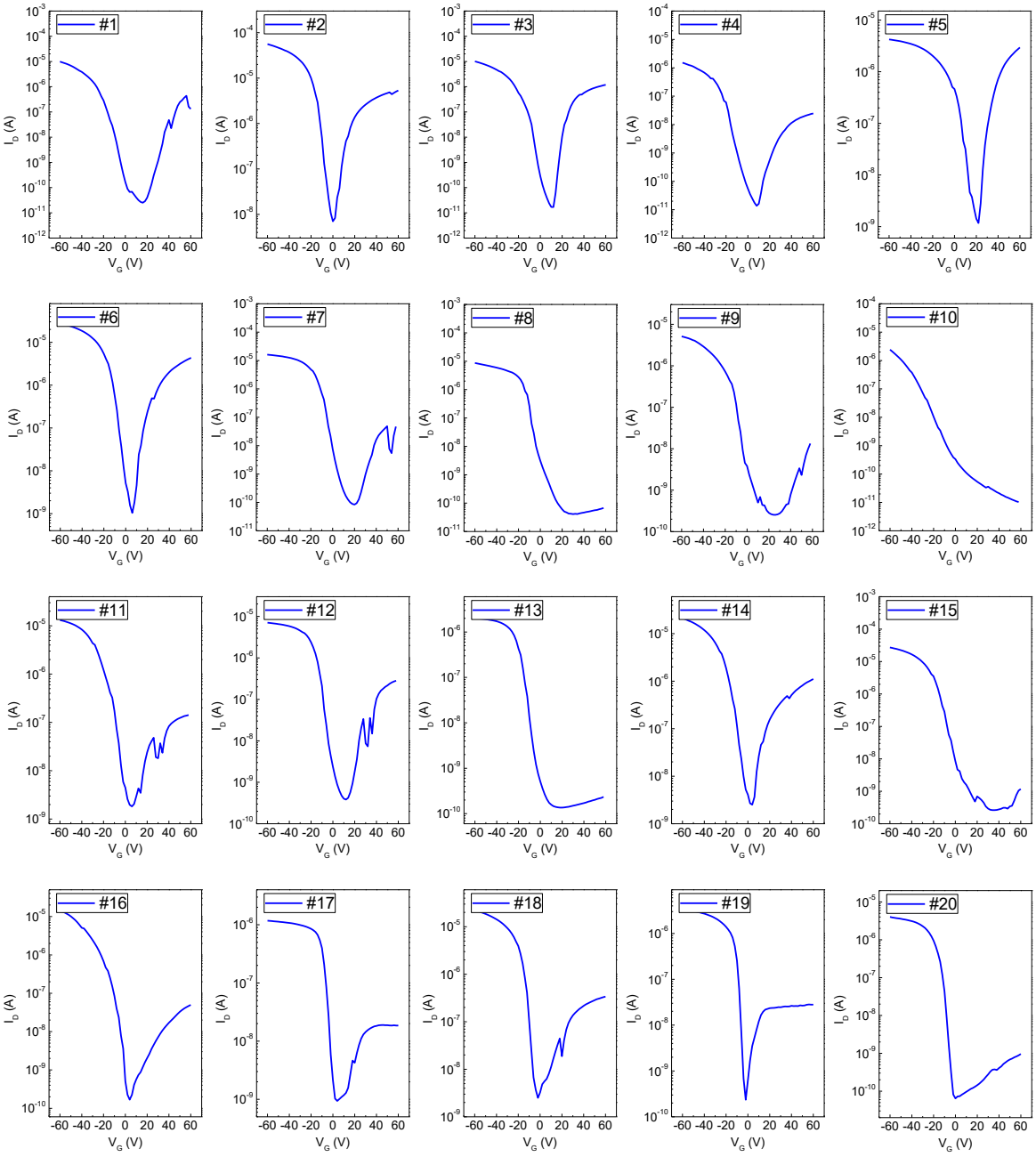

Figure S8. Transfer characteristics of 20 baseline WSe_2 transistors.

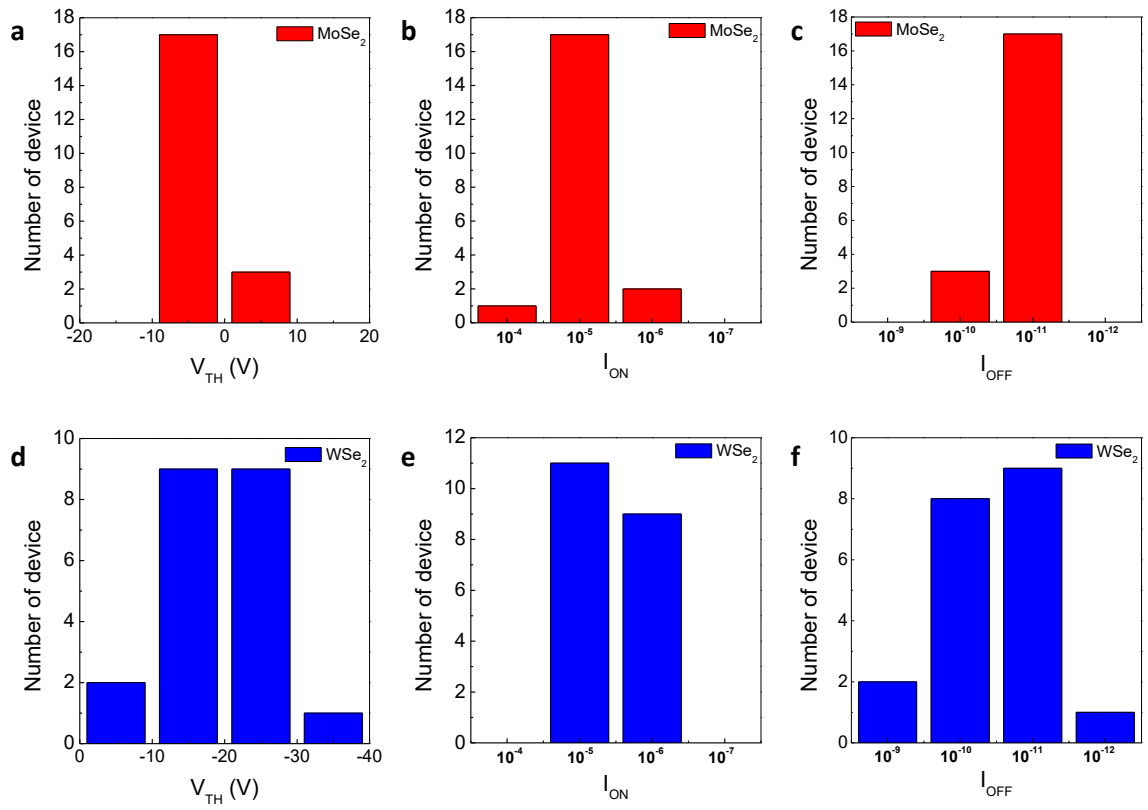

Figure S9. Statistical analysis of 20 baseline $MoSe_2$ and 20 baseline WSe_2 transistors. Histogram distribution of (a) V_{TH}, (b) I_{ON}, and (c) I_{OFF} of the 20 baseline $MoSe_2$ transistors. (d) V_{TH}, (e) I_{ON}, and (f) I_{OFF} of the 20 baseline WSe_2 transistors.

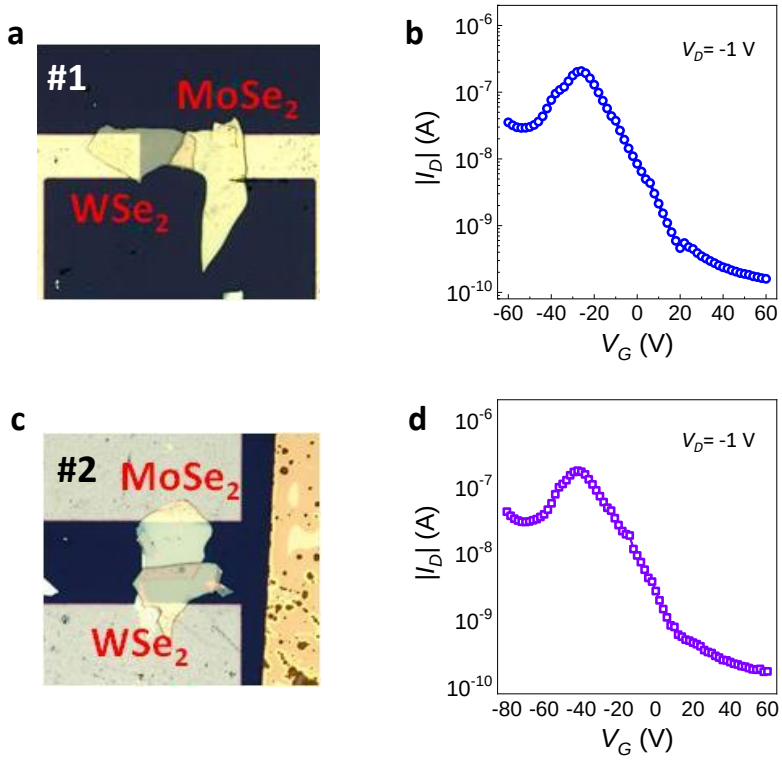

Figure S10. Investigations of multiple $MoSe_2$–WSe_2 vdW-H-TRs. a) Optical microscopy image and b) Transfer characteristics of the $MoSe_2$-WSe_2 vdW-H-TR (device #1) for $V_D = -1$ V. c) Optical microscopy image and d) Transfer characteristics of the $MoSe_2$-WSe_2 vdW-H-TR (device #2) for $V_D = -1$ V.

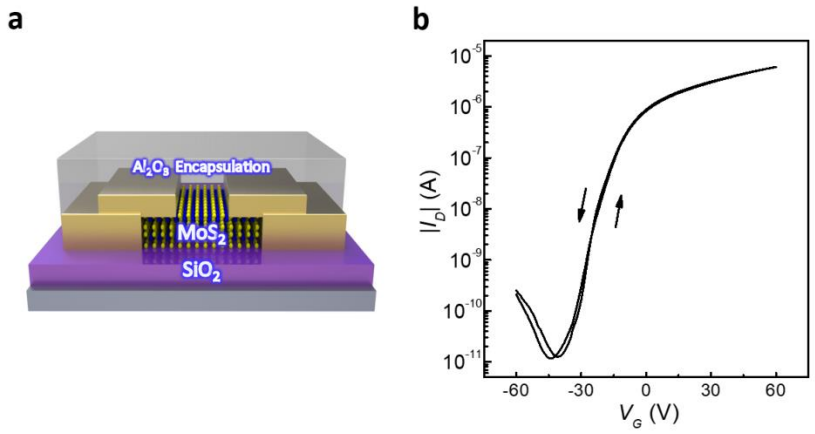

Figure S11. **Forward and reverse sweeps plot of MoS_2 transistor without floating-gate.** a) 3D Schematic structure of the MoS_2 H-TR. b) Transfer characteristics of the MoS_2 transistor.

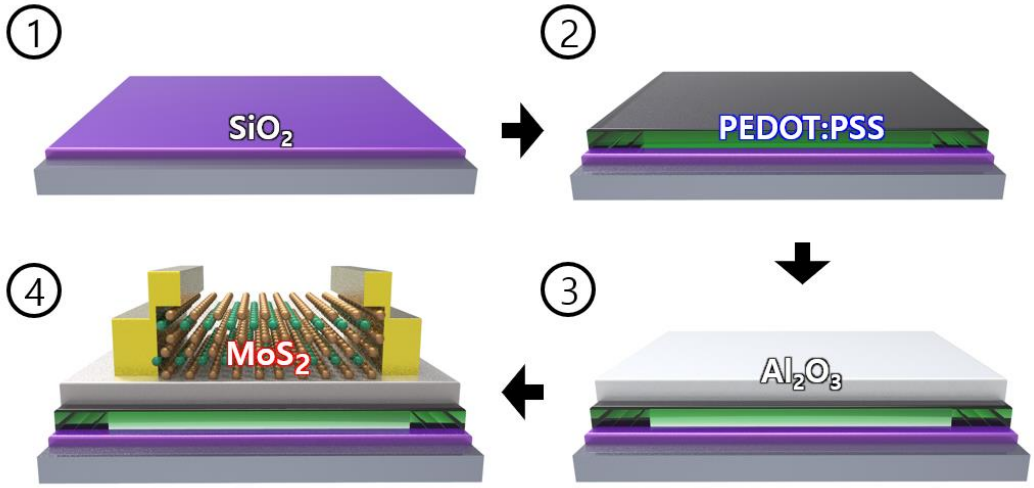

Figure S12. N-type MoS_2 floating-gate transistor fabrication process flow. We deposited PEDOT: PSS solution on top of SiO_2 substrate and sequentially deposited 80 nm thick Al_2O_3 by atomic layer deposition (ALD). And then, Au/Ti (100 nm/20 nm) as contact electrode was deposited on top of mechanically exfoliated MoS_2 layer.

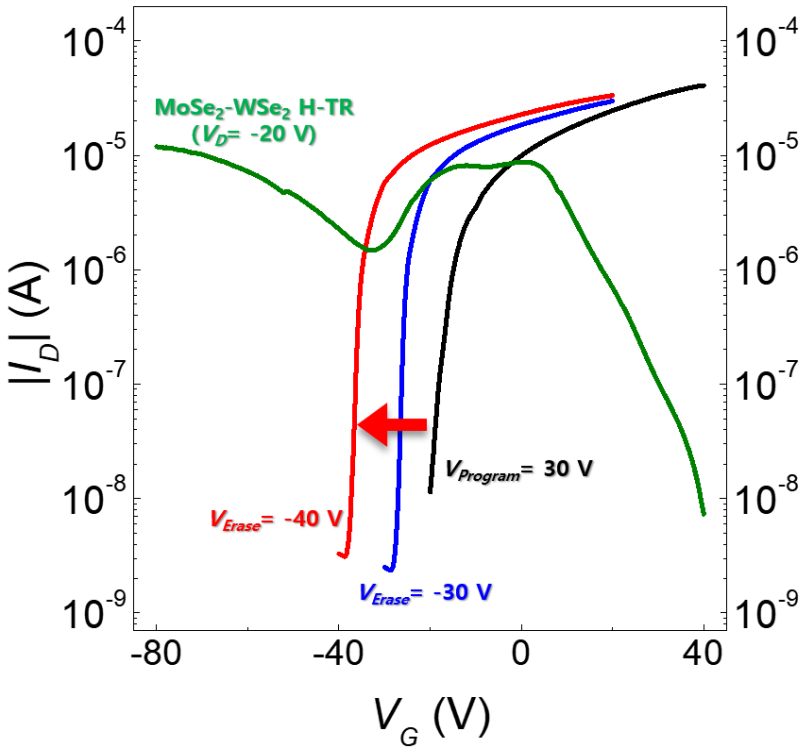

Figure S13. Comparison of transfer curves of the $MoSe_2$-WSe_2 vdW-H transistor (green curve for V_D= −20 V) and MoS_2 floating-gate transistor (black curve for $V_{Program}$= 30 V, blue curve for $V_{Program}$= -30 V and red curve for V_{Erase}= −40V).

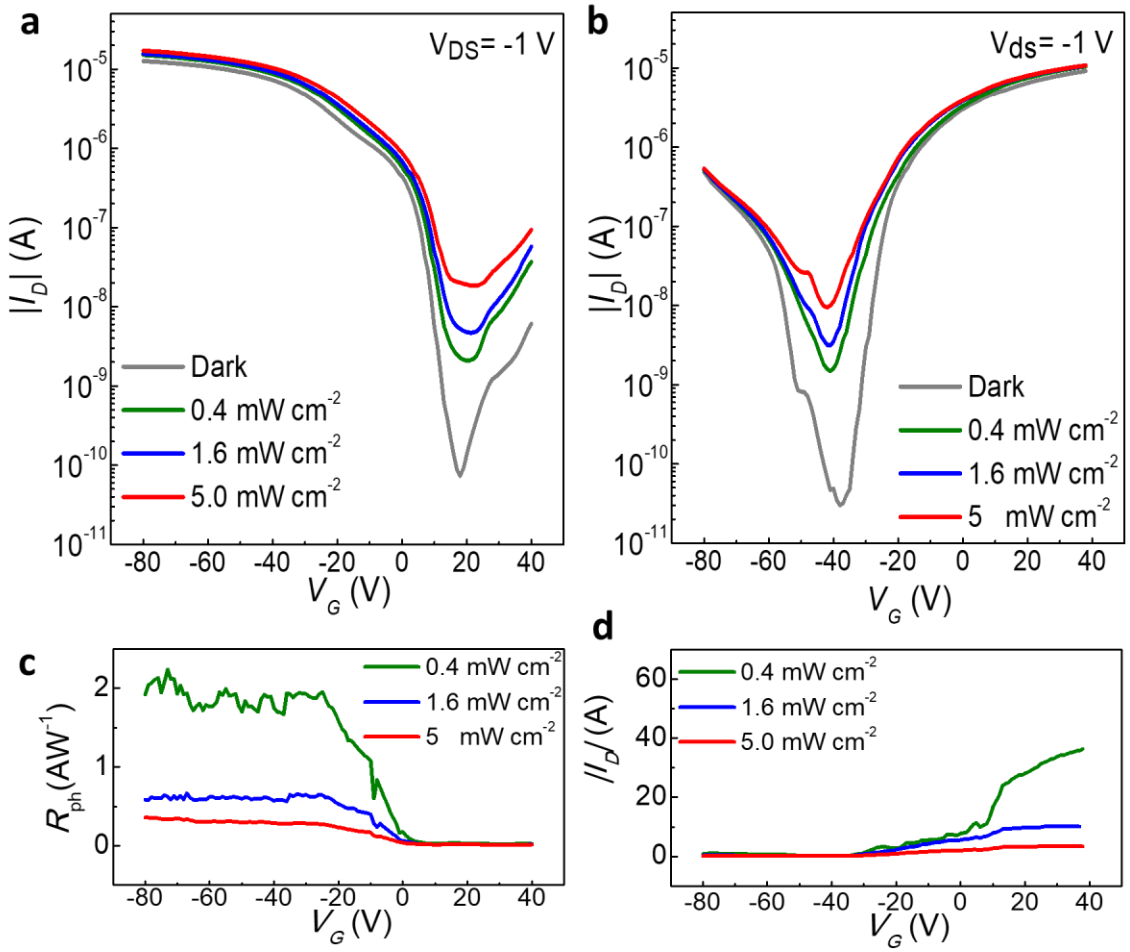

Figure S14. Photoresponsive characteristics of the baseline $MoSe_2$ and baseline WSe_2 transistors for $V_D = -1$ V. Transfer characteristics of a) $MoSe_2$ transistor and b) WSe_2 transistor under illumination for $V_D = -1$ V (P_{inc} = 0.4, 1.6, and 5.0 mW cm^{-2}, and λ_{ex} = 638 nm). Calculated photoresponsivity of c) $MoSe_2$ transistor, and b) WSe_2 transistor.

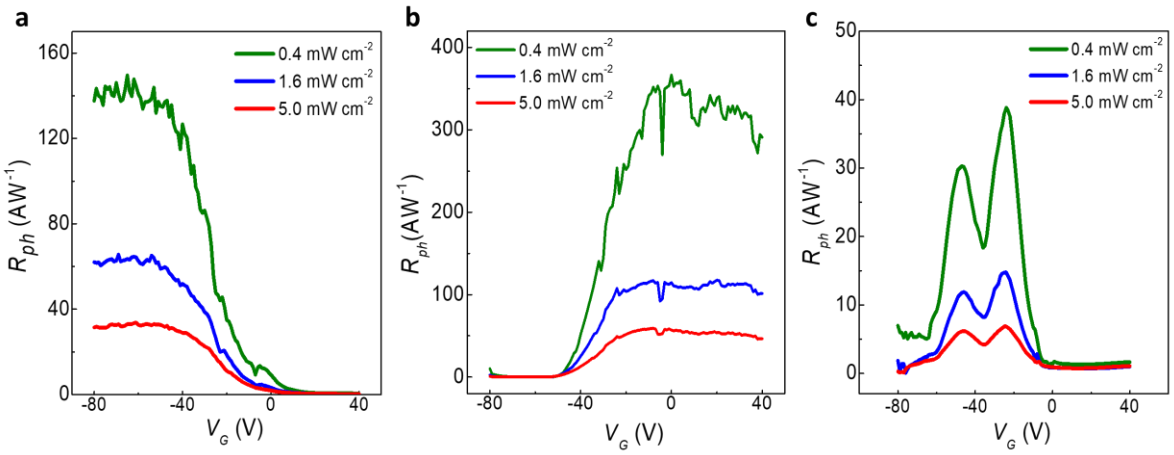

Figure S15. Phororesponsivity (R_{ph}) of a) baseline WSe_2 transistor b) baseline $MoSe_2$ transistor c) $MoSe_2$-WSe_2 vdW-H-TR as a function of V_G.

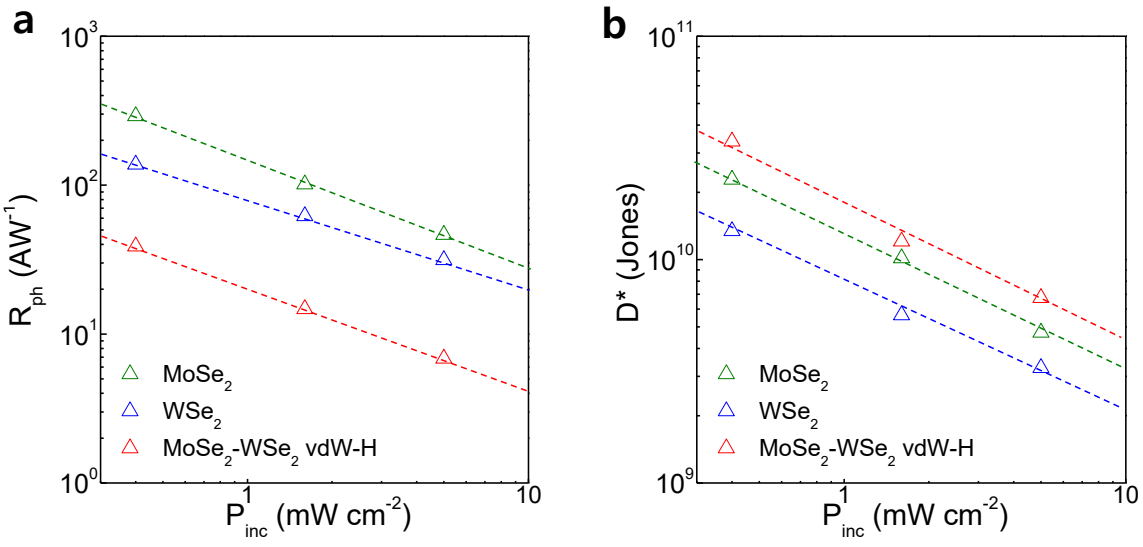

Figure S16. a) Photoresponsivity (R_{ph}) and b) specific detectivity (D*) of the baseline WSe_2, baseline $MoSe_2$, and $MoSe_2$-WSe_2 vdW-H-TR.

References

1. Liu, H., Neal, A. T. & Ye, P. D. Channel length scaling of MoS_2 MOSFETs. *ACS Nano* **6**, 8563-8569 (2012).
2. Zhao, W. et al. Lattice dynamics in mono-and few-layer sheets of WS_2 and WSe_2. *Nanoscale* **5**, 9677-9683 (2013).
3. Wang, X. et al. Pressure-induced iso-structural phase transition and metallization in WSe_2. *Sci. Rep.* **7**, 46694 (2017).
4. Nam, D., Lee, J.-U. & Cheong, H. Excitation energy dependent Raman spectrum of $MoSe_2$. *Sci. Rep.* **5**, 17113 (2015).
5. Ambrosi, A., Sofer, Z. & Pumera, M. 2H→ 1T phase transition and hydrogen evolution activity of MoS_2, $MoSe_2$, WS_2 and WSe_2 strongly depends on the MX_2 composition. *ChemComm* **51**, 8450-8453 (2015).
6. Rohaizad, N., Mayorga-Martinez, C. C., Sofer, Z. k. & Pumera, M. 1T-phase transition metal dichalcogenides (MoS_2, $MoSe_2$, WS_2, and WSe_2) with fast heterogeneous electron transfer: application on second-generation enzyme-based biosensor. *ACS Appl. Mater. Interfaces* **9**, 40697-40706 (2017).